

TacTID: High-Performance Visuo-Tactile Sensor-Based Terrain Identification for Legged Robots

Ziwu Song^{ID}, Chenchang Li, *Graduate Student Member, IEEE*, Zhentan Quan^{ID}, Shilong Mu, Xiaosa Li^{ID}, *Graduate Student Member, IEEE*, Ziyi Zhao, Wanxin Jin^{ID}, Chenye Wu^{ID}, *Senior Member, IEEE*, Wenbo Ding^{ID}, *Member, IEEE*, and Xiao-Ping Zhang^{ID}, *Fellow, IEEE*

Abstract—Adapting to various terrains and improving locomotion performance have always been challenging for legged robots. Inspired by the animal somatosensory system in walking and balancing, the robot can benefit from the foot sensors as well when interacting with the terrain and gain better performance. In this article, we propose a visuo-tactile foot sensor with embedded markers, named TacTID, for legged robot terrain identification. By introducing elastic embedded markers on an elastic hemispherical shell, TacTID could detect 3-D pressure distribution directly, based on which the terrain coefficient of sliding friction (COSF) and terrain effective stiffness can be estimated precisely. The results of the COSF prediction experiment demonstrate that TacTID exhibits an average error of 0.036, which is notably lower than that of TacTip. For the effective stiffness estimation experiment, TacTID is tested on ten silicone cubes with different Young's moduli, and the absolute average estimation error is less than 0.1 MPa. Besides, a quadruped robot is equipped with TacTID for real-time terrain identification, and the possibility to estimate COSF and the terrain effective stiffness in various terrains is demonstrated. This research highlights the potential of TacTID for robotic applications requiring precise contact force and terrain identification in real-time.

Index Terms—Legged robot, tactile sensing, terrain identification.



Manuscript received 11 June 2024; accepted 13 June 2024. Date of publication 27 June 2024; date of current version 15 August 2024. This work was supported in part by Shenzhen Science and Technology Program under Grant JCYJ20220530143013030, in part by Guangdong Innovative and Entrepreneurial Research Team Program under Grant 2021ZT09L197, and in part by Shenzhen Institute of Artificial Intelligence and Robotics for Society and Meituan. The associate editor coordinating the review of this article and approving it for publication was Prof. Mohsen Asadnia. (Ziwu Song and Chenchang Li contributed equally to this work.) (Corresponding author: Wenbo Ding.)

Ziwu Song, Chenchang Li, Zhentan Quan, Shilong Mu, Xiaosa Li, and Ziyi Zhao are with Shenzhen International Graduate School, Tsinghua University, Shenzhen 518071, China (e-mail: song-zw20@mails.tsinghua.edu.cn; li-cc21@mails.tsinghua.edu.cn; qzt21@mails.tsinghua.edu.cn; msl22@mails.tsinghua.edu.cn; lixs21@mails.tsinghua.edu.cn; zy-zhao21@mails.tsinghua.edu.cn).

Wanxin Jin is with the School for Engineering of Matter, Transport, and Energy, Arizona State University, Tempe, AZ 85287 USA (e-mail: wanxinjin@gmail.com).

Chenye Wu is with the School of Science and Engineering, Chinese University of Hong Kong, Shenzhen 518172, China (e-mail: chenye.wu@yeah.net).

Wenbo Ding and Xiao-Ping Zhang are with Shenzhen International Graduate School, Tsinghua University, Shenzhen 518071, China, and also with the RISC-V International Open Source Laboratory, Shenzhen 518055, China (e-mail: ding.wenbo@sz.tsinghua.edu.cn; xiaoping.zhang@sz.tsinghua.edu.cn).

This article has supplementary downloadable material available at <https://doi.org/10.1109/JSEN.2024.3417514>, provided by the authors.

Digital Object Identifier 10.1109/JSEN.2024.3417514

1558-1748 © 2024 IEEE. Personal use is permitted, but republication/redistribution requires IEEE permission.

See <https://www.ieee.org/publications/rights/index.html> for more information.

Authorized licensed use limited to: Harbin Institute of Technology. Downloaded on September 16, 2024 at 06:54:16 UTC from IEEE Xplore. Restrictions apply.

I. INTRODUCTION

LEGGED robots have attracted increasing interest in recent years due to their ability to traverse rough terrain and perform various tasks such as search and rescue, exploration, and military operations [1], [2]. Some terrain information, such as friction, stiffness, slope, and irregular obstacle, affect the legged robot's mobility performance. However, the traditional vision-based terrain identifications rely heavily on the light condition and are limited in the field of view [3], which hardly captures accurate terrain information, especially under scenarios with unstructured terrains. Consequently, in practice, a good terrain sensing and adaptation system is desired for legged robots.

To enhance their adaptability to unstructured terrain, it is crucial for legged robots to improve their perception of ground information. This enhancement facilitates their ability to navigate and operate effectively in diverse and unpredictable environments. Some previous works improved the tactile sensor's ability to detect changes in the terrain properties by equipping legged robots with foot tactile sensors [4], [5], [6]. Optical sensors are commonly used in high-precision and high-resolution sensing scenarios due to their high sensitivity and low cost [7], [8]. However, the resolution of most sensors in

these previous works still cannot provide sufficient information for sensing complex terrains [9], [10], [11], [12].

Thanks to the powerful computer vision algorithms, the visuo-tactile sensors have emerged as effective tactile sensing solutions of high resolution and accuracy [13], [14], [15]. A visuo-tactile sensor called TacTip [16], [17] owns impressive capabilities in detecting contact pressure and approximating 3-D geometry of a touched surface by analyzing the deformation of markers inside the sensor. Cramphorn et al. [18] first used the Voronoi diagram tessellation algorithm to infer the normal and tangential pressure directly with TacTip, but the algorithm complexity is $\mathcal{O}(n \log n)$ with optimization [19] and not time-efficient. To explore the importance of tactile sensing on robot stabilizing on different terrains, Zhang et al. [20] proposed a foot visuo-tactile sensing system that augments a tailored single-legged robot. They used an optical flow algorithm and convolutional neural networks to detect marker displacements and use real-time feedback control to achieve stabilization. Stone et al. [21] equipped a quadruped robot with a single TacFoot sensor, and the sensor enabled the robot to walk along a narrow beam by detecting the beam's edges. However, a notable limitation of the aforementioned these two works is their suboptimal real-time performance. Zhang et al. [20] showed that the angular velocity of the single-legged robot is less than $1^\circ/\text{s}$. Similarly, with the single TacFoot sensing system [21], the quadruped movement speed was less than 0.03 m/s , with only one quadruped foot replaced with a TacFoot sensor.

Since the friction and effective stiffness are significant terrain properties affecting the legged robot's mobility performance and sensing these properties in real-time is still a challenge, this article proposes a visuo-tactile foot sensor named TacTID, designed to aid legged robots in real-time terrain identification by estimating the coefficient of sliding friction (COSF) and effective stiffness of the terrain (Fig. 1). With TacTID sensing the 3-D pressure distribution, COSF of the terrain can be predicted by estimating the linear boundary of the friction cone [22], and the terrain effective stiffness can also be determined by predicting the contact area radius according to the Hertzian contact theory [23]. Effective stiffness directly reflects the relationship between deformation and load when two deformable bodies are in contact [24], which is crucial information in the control of robots with soft structures [25]. The experiments conducted on a Unitree Go1 demonstrate that TacTID can accurately learn COSF and effective stiffness information across various surfaces, indicating the potential of vision-based tactile sensors in enhancing the locomotion of legged robots.

The main contributions of this work are trifold.

- 1) A high-performance tactile sensor called TacTID with elastic embedded markers is designed, fabricated, and evaluated, which can estimate the 3-D pressure distribution directly.
- 2) We propose terrain identification methods estimating the COSF and effective stiffness of the terrain in real-time, based on the data of TacTID.
- 3) By equipping the quadruped robot with four TacTIDs, we demonstrate real-time terrain identification across

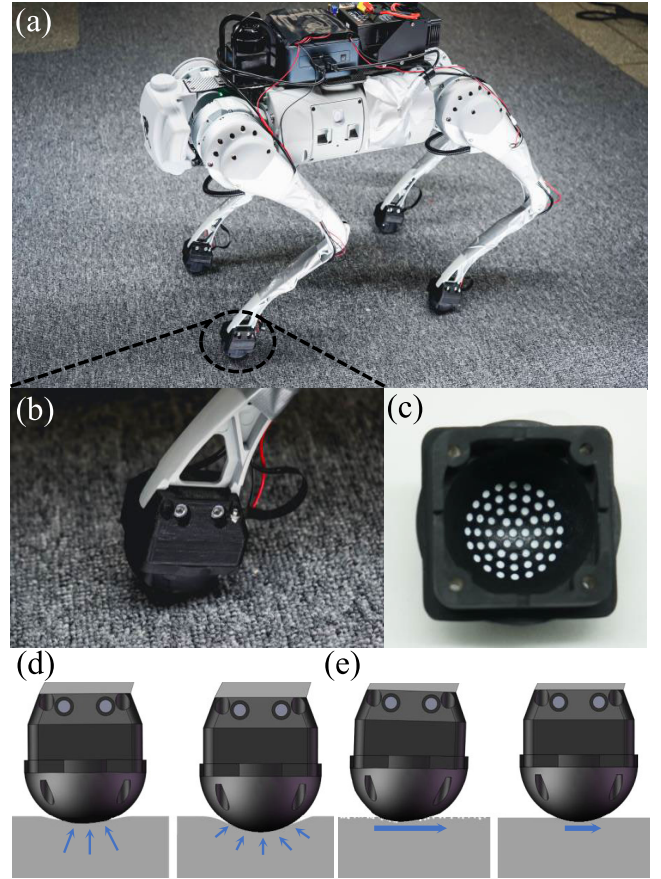


Fig. 1. Schematic illustration of TacTID mounted on quadruped's feet. (a) Unitree Go1 equipped with four TacTIDs. (b) Outside view of TacTID. (c) Inside view of the TacTID. (d) Schematic of the TacTID contacting with surfaces owing different effective stiffness. (e) Schematic of the TacTID contacting with surfaces owing different COSF.

different locomotion modes, including walking and trotting.

II. SYSTEM DESIGN

The proposed TacTID sensor is custom-built to replace the foot of Unitree Go1, with details introduced as follows.

A. Tactile Sensor

1) *Sensor Design:* The TacTID features an elastic hemispherical shell with an inner surface radius of 17.5 mm and an outer surface radius of 22.5 mm. Different from the design of TacTip [26], the proposed TacTID uses an elastic embedded marker array to replace the pin array [Fig. 2(a)], which has a greater area change ratio than the pins of TacTip and achieves higher normal pressure sensitivity. Here, each marker has a shape of hemispheric with a radius of 1 mm and the center is located on the inner surface of the shell. When the outer surface is pressed, the elastic embedded markers deform with the whole shell. Because the area and position in the image of each marker change during the deformation, displacements along the z -axis can be determined by computing the area change ratio of each marker. Meanwhile, displacements along the x - and y -axes can be determined by tracking the centers of markers. The inside camera is OV5693 with a size of $10 \times 10 \text{ mm}$, an unadjustable 1.78-mm focal length, a field of view

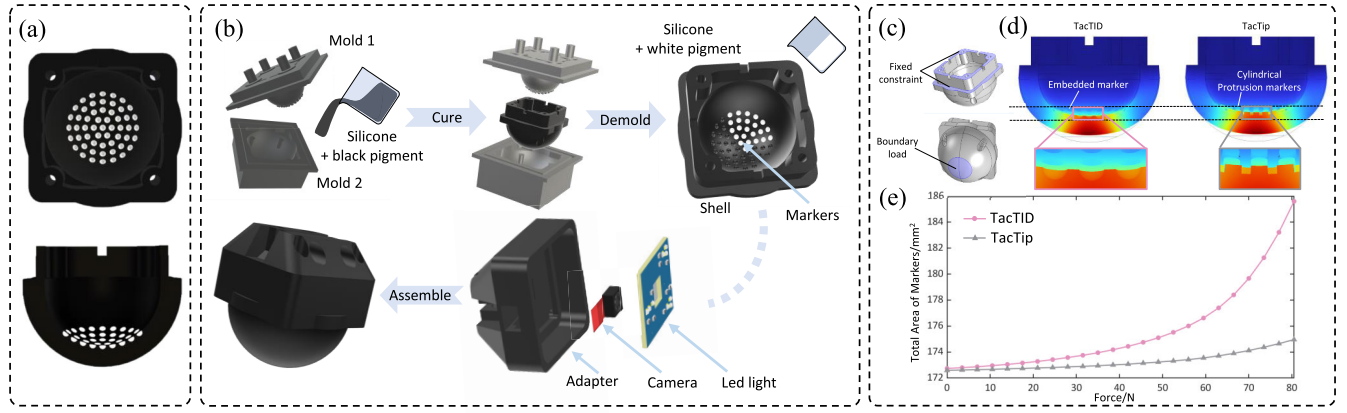


Fig. 2. (a) Inside view and cross section view of the TacTID marker array. (b) Whole silicone curing process and assembling process of TacTID. (c) Geometric model used in simulation. (d) Deformation results in simulation of both TacTID and TacTip. (e) Observed area change in all the markers in the simulation of both TacTID and TacTip.

of 120°, a maximum frame rate of 60 Hz, and a resolution of 640 × 480. The light board and camera are pasted on the lower face of the adapter. The light board has dimensions of 34 × 22 mm with a square hole of 10 × 10 mm. It has three evenly distributed white light-emitting diodes (LEDs) that uniformly illuminate the white markers in TacTID.

2) Sensor Fabrication: Fig. 2(b) depicts the whole fabrication process of TacTID, which features a dual-stage casting process. In the first stage, the mixture of the silicone and the black pigment is poured into Mold1 and then covered by Mold2 to cast the elastic hemispherical shell. After curing the shell, there is a pit array evenly distributed on the inner surface of the shell. In the following stage, silicone with white pigment is filled into the pit array and cured to form the elastic embedded marker array, which can deform along with the elastic hemispherical shell. The elastic hemispherical shell is designed to mate an adapter for reliable and firm installation, and the adapter is fabricated via polylactic acid 3-D printing, which is used to install the sensor to the experimental platform conveniently, and also provides mounting points for the camera and LED light board.

3) Finite Element Simulation: The area change responses of the markers in both TacTID and TacTip are simulated in COMSOL to validate the design advancements. In the simulation, the TacTID model has elastic embedded markers with a Young's modulus of 0.621 MPa, while the TacTip model has cylindrical pin markers and has the same hemispherical shell as TacTID. TacTID shares identical simulation parameters with TacTip. Both the simulations use a Young's modulus of 8.175 MPa, a Poisson's ratio of 0.49, and a density of 1.5 kg/m³. As shown in Fig. 2(c), the fixed constraint region is defined as the contact location between the sensor and the adaptor. The boundary load region is set to be a circular area of approximately 1 cm² on the outer surface of the elastic hemispherical shell of TacTID or TacTip. Normal forces ranging from 0 to 80 N are applied to an area of edge load area on the outer surface of both the sensors, and the total area of all the markers is observed. The simulation results, as illustrated in Fig. 2(d) and (e), reveal that the markers on TacTID expand significantly more than those on TacTip, thus demonstrating that TacTID is more sensitive to normal force compared with the traditional TacTip. When subjected to the

same load, both the inner surfaces of TacTID and TacTip undergo tensile expansion. However, the tensile strain on the pin markers at the top of TacTip is smaller than that at the bottom, due to its higher Young's modulus and smaller surface area expansion.

B. Feature Extraction

When TacTID experiences contact from an external force, the markers on the sensor's surface shift and expand due to the deformation of the elastic hemispherical shell. The main goal of feature extraction is to detect and track these markers, calculating their displacement along the x - and y -axes and the area change ratio. Before detecting and identifying the markers, the image undergoes typical preprocessing with OpenCV, including image filtering, morphological processing, and contour detection. To track each marker contour, the contours in an image frame are assigned indexes as the identification, and the identification in the first frame is used as the reference. The contours in subsequent frames are matched to those of the reference frame using the Euclidean distance and the Hungarian algorithm [27]. With n representing the number of the markers, the area change ratio of the i th frame on the j th contour area $\eta_i = [\eta_{i,1}, \eta_{i,2}, \dots, \eta_{i,n}]$ is defined by

$$\eta_{i,j} = \frac{a_{i,j} - a_{1,j}}{a_{1,j}}, \quad 1 \leq j \leq n \quad (1)$$

where $a_{i,j}$ is the j th contour area in the i th frame, and the first frame is chosen as the reference. Similarly, the displacements along the x - and y -axes, which are represented as $\mathbf{u}_i = [u_{i,1}, u_{i,2}, \dots, u_{i,n}]$ and $\mathbf{v}_i = [v_{i,1}, v_{i,2}, \dots, v_{i,n}]$, are computed. In Fig. 3(a), \mathbf{u}_i , \mathbf{v}_i , and the resultant displacement of each marker are indicated by green, blue, and red arrows, respectively, while η_i is visualized as the brightness of each contour. For a denser area change ratio and displacement field, the linear interpolation is used on η_i , \mathbf{u}_i , and \mathbf{v}_i separately within a regular grid of size 100 × 100, and the result of interpolated η_i is shown in Fig. 3(b). It can be seen from Fig. 3(c) and (d) that when TacTID deforms due to a contact force, the visualized 3-D deformation can be constructed with the interpolated results.

To validate the effectiveness of TacTID's feature extraction, we measure the processing time required for this step and

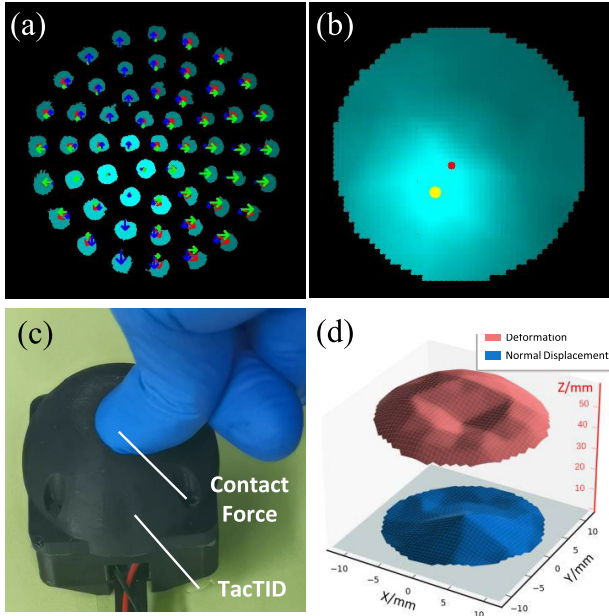


Fig. 3. Visualized feature extraction results on TacTID. (a) Displacement and area change ratio are shown. (b) Denser area change ratio after linear interpolation. (c) TacTID is deformed by a contact force. (d) Three-dimensional reconstruction based on the interpolated results.

TABLE I
TIME CONSUMPTION COMPARISON

Method	Feature extraction time
OF-based [20]	12 ms
Voronoi-based [18]	9 ms
Ours	1 ms

compare it to the existing methods. As shown in Table I, our feature extraction method, which incorporates embedded markers, exhibits the shortest processing time. Specifically, the OF-based approach [20] uses optical flow for tracking x and y displacements, while the Voronoi-based method [18] uses the computation of the Voronoi diagram to ascertain normal pressure.

C. Characterization

As shown in Fig. 4(a), a probe is connected to a three-axis force/torque sensor (M3733C Sunrise Instruments) to monitor the contact force, and the probe is mounted on a robot arm with a positioning error of less than 0.1 mm. During each characterization experiment, the robot arm carries the probe toward the set position on TacTID at a constant speed of 10 mm/s until the contact force feedback from the force sensor reaches the predetermined value. Once the force sensor detects that the target force has been achieved, the robot arm stops. Then the probe remains in place for 5 s before the robot arm returns to its original position. The whole process is repeated ten times for each position and force, ensuring a robust and reliable characterization.

The normal force characterization experiment involves selecting ten different pressing positions, ranging from 0 to 9 mm with a step of 1 mm. The Unitree Go1 in Fig. 1(a) equipped with TacTID, an Intel NUC, and a lithium battery has a total weight of 12.23 kg. Considering that at least two feet are in contact with the terrain during both walking and trotting gaits, the load on a single TacTID remains within 60 N.

Accounting for additional impact during foot–terrain contact, the contact pressure applied on TacTID during the quadruped’s walking falls within the range of 0–80 N. The pressing characterization experiment is conducted using a pressure range of 0–80 N. A similar process is conducted during tangential force characterization, and the contact positions also range from 1 to 9 mm, and the force range is 0–80 N. In Fig. 4(b), the characterization results with contact force increasing from 25 to 75 N and the distance from the center increasing from 0 to 6 mm are illustrated. It can be seen that the area change ratio slightly decreases as the contact position varies at the same pressure level, while the rate increases as the pressing force increases at the same position. Based on the characterization results, three mappings from TacTID raw data to mechanics quantities are established using three simple fully connected neural networks [28], \mathbf{H}_N , \mathbf{H}_T , and \mathbf{H}_p

$$F_{N,i} = \mathbf{H}_N(\eta_i) \quad (2)$$

$$F_{T,i} = \mathbf{H}_T(\mathbf{u}_i, \mathbf{v}_i) \quad (3)$$

$$\mathbf{p}_i = \mathbf{H}_p(\eta_i) \quad (4)$$

where $F_{N,i}$ and $F_{T,i}$ are the normal and tangential forces, respectively, and \mathbf{p}_i is the normal pressure distribution along the z -axis.

The same characterization experiment is conducted on the TacTip, the marker of which is a cylindrical protrusion with a diameter and height of 1 mm. In Fig. 4(b), the area change ratio of TacTID is about twice that of TacTip under the same condition, indicating that TacTID is more sensitive to the normal force. The results of the characterization experiment on tangential force show similar sensitivities on TacTID and TacTip [Fig. 4(c)].

III. TERRAIN IDENTIFICATION METHODS

After the characterization of normal and tangential forces, the TacTID is then used for terrain identification. In this part, the COSF and effective stiffness of the contact terrain are estimated based on the extracted features.

A. Friction Coefficient Estimation Method

One difficulty is the variation in the normal force between the foot and the terrain, which results in a varying tangential force that cannot be directly used to calculate COSF. In addition, the necessity to differentiate between slipping and sticking contact makes COSF estimating for quadruped robots more challenging. Here, a statistical fitting method based on the friction cone theory [22] is adopted to estimate the COSF from real-time data. The normal and tangential force output by TacTID in each frame of the image is regarded as a sample point. By fitting the linear boundaries of sample points output by multiple frames of images, the fit boundary slope is considered as the COSF. By denoting a sample as $\mathbf{s}_i = [F_{T,i}, F_{N,i}]$, the estimation process begins by collecting a set of m samples $\{\mathbf{s}_1, \mathbf{s}_2, \dots, \mathbf{s}_m\}$ from m image frames, and all the samples are considered to locate in a friction cone area, while the samples of sliding friction are on the friction boundary. Because the ratio, $F_{T,i}/F_{N,i}$, of sliding friction is lower than that of sticking friction, samples with m' lowest $F_{T,i}/F_{N,i}$ are selected to eliminate the noise introduced by

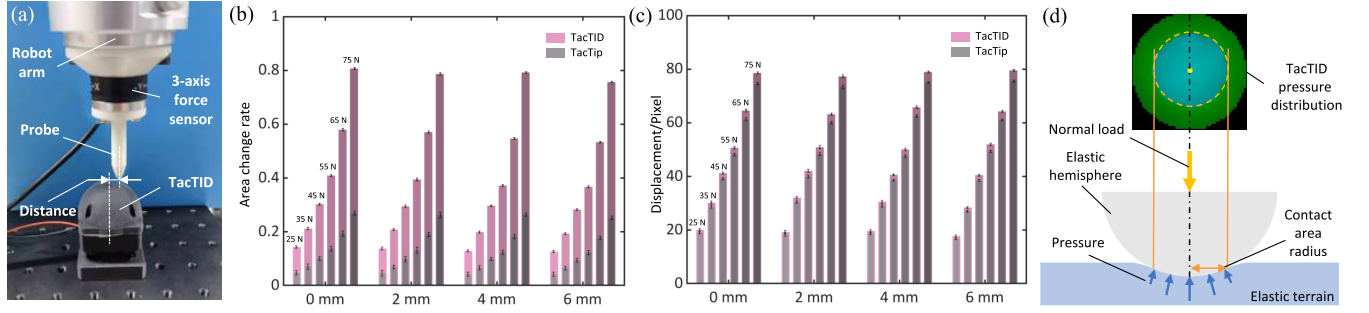


Fig. 4. (a) Characterization experiment setup. (b) Marker area change ratio of the sensors with different contact forces and contact locations. (c) Average displacement in pixels of the sensors with different contact forces and contact locations. (d) Schematic representation of elastic hemisphere and elastic terrain.

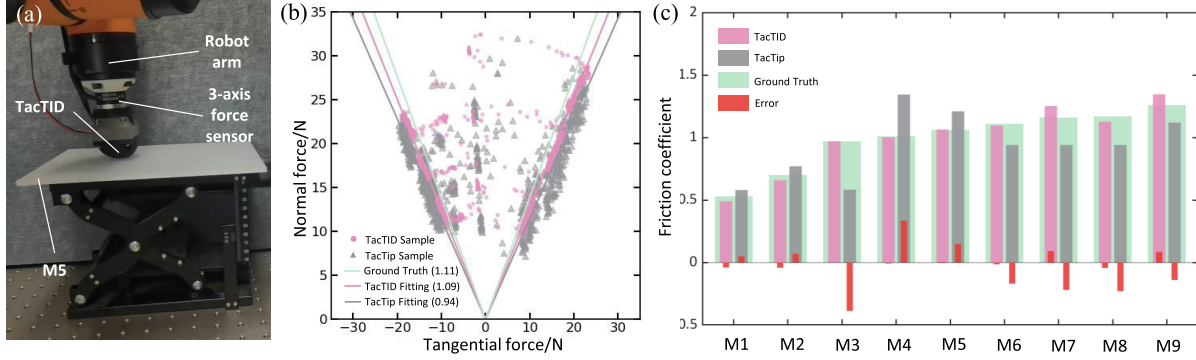


Fig. 5. (a) COSF estimation experimental setup. (b) Friction cone boundaries' fitting result of both TacTID and TacTip on M6. (c) Comparison of the COSF estimation between TacTID and TacTip.

sticking friction. The hyperparameter m' is set empirically as $m' = m/3$. The random sample consensus (RANSAC) method [29] is applied to further remove the effect of the sticking friction. Subsequently, the COSF is estimated using the least-squares method by fitting the samples located on the friction cone boundary.

B. Effective Stiffness Estimation Method

The study of the interactions between an elastic spherical shell and an object remains incomplete [30]. Numerous researchers have explored the elastic contact of various bodies with a spherical object [31], [32], [33]. We characterize the interaction between TacTID and the terrain mathematically using the Hertzian contact theory [23], [32]. This theory is well-established and provides a solution for scenarios in which an elastic spherical body contacts with an elastic plane, as illustrated in Fig. 4(d). Within the context of Hertzian contact, the theoretical normal pressure distribution can be computed by [33]

$$\tilde{\mathbf{p}}_i(x, y) = p_0 \left(1 - \frac{x^2 + y^2}{r_i^2} \right)^{\frac{1}{2}}. \quad (5)$$

Here, p_0 corresponds to the maximum contact pressure resulting from the applied normal force $F_{N,i}$, and r_i represents the contact area radius in the i th image frame, which are indicated in Fig. 4(d). Besides, x and y represent the position with respect to the center of TacTID in the image. We also introduce the theoretical normalized normal pressure distribution as $\hat{\mathbf{p}}_i(x, y) = \tilde{\mathbf{p}}_i(x, y)/p_0$. To estimate the terrain effective stiffness via the data of TacTID, $F_{N,i}$ and r_i should

be determined beforehand. Here, $F_{N,i}$ is computed according to (2). Based on the dense pressure distributed \mathbf{p}_i in (4), the contact area radius r_i can be estimated by optimizing the error of estimated normal pressure distribution

$$r_i = \arg \min_{r_i} \|\mathbf{p}_i - \hat{\mathbf{p}}_i\|_2 \quad (6)$$

which is a convex optimization problem. Furthermore, the relationship between normal force $F_{N,i}$ and the radius of the contact area r_i can be modeled by [32]

$$E_i = \frac{3RF_{N,i}}{4r_i^3} \quad (7)$$

where E_i is the effective Young's modulus of the whole system composed of TacTID and terrain, which is related to Young's modulus and Poisson's ratio of both TacTID and the terrain. Considering that the outer radius of TacTID, R is known and constant, the relationship is determined solely by E_i . The effective stiffness of a material is related to its resistance to deformation or indentation. Hence, according to (7), the estimated effective Young's modulus in the i th frame can be calculated, which is a measure of the terrain effective stiffness.

IV. EXPERIMENTS

The friction coefficient estimation experiment evaluates the performance of TacTID in estimating COSF using the proposed COSF estimation method. The effective stiffness estimation experiment assesses TacTID's performance in estimating terrain effective stiffness using the proposed effective stiffness estimation method. In addition, four TacTIDs are deployed on a quadruped robot to demonstrate the real-time performance in estimating terrain COSF and effective stiffness.

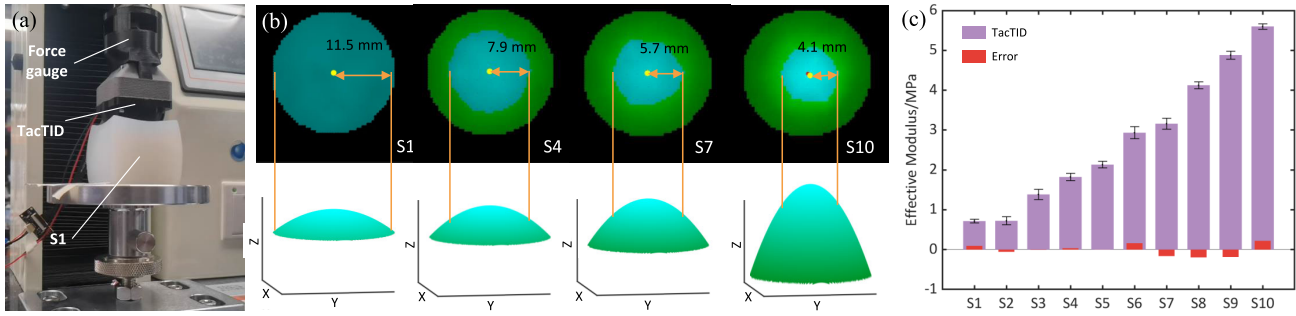


Fig. 6. (a) Effective stiffness estimation experimental setup. (b) Estimated contact area and theoretical normal pressure distribution. (c) Effective Young's modulus estimation results of TacTID and corresponding errors.

A. Friction Coefficient Estimation

The experiment aims to verify TacTID's ability to perceive COSF and evaluate the accuracy in sensing different surfaces with varying COSFs. In this experiment, nine materials were used, these were ice surface, wet acrylic, carpet, polyvinyl chloride, wood, paper, aluminum-plastic, acrylic, and nylon, which are denoted using M1, M2, ..., M9, respectively. Real-time normal and tangential forces are collected using the three-axis force/torque sensor to calculate the ground truth of COSFs. As shown in Fig. 5(a), the aforementioned materials are mounted tightly on an optical platform to reduce the effect of the relative slide between the platform and the material. A three-axis force/torque sensor is mounted at the end of the robot arm to assist in setting the contact force of the arm, and TacTID is connected to the three-axis force/torque sensor.

In each trial, the robot arm drives TacTID to press the target material along the vertical direction at the starting position. After the pressure reaches the target value, the normal displacement stops, and the arm moves horizontally with an acceleration of 10 mm/s^2 and a maximum speed of 20 mm/s . The total sliding distance is 270 mm . Before the robot arm reaches the endpoint, it decelerates at an acceleration of -10 mm/s^2 and precisely stops at the set endpoint. During the experiment, TacTID outputs real-time normal and tangential forces. The TacTID samples collected on M4 of static and sliding friction differentiated by the RANSAC method are shown in Fig. 5(b). The sliding friction samples are fit with the least-squares method to obtain the fitting line slope whose absolute value is regarded as COSF, while the same experimental steps are also carried out with the TacTip.

Figs. 2(e) and 4(b) illustrate that TacTip has lower sensitivity and stability compared with TacTID in sensing normal force, which results in significant errors when TacTip is used for COSF estimation. As shown in Fig. 5(b), considering that both the gray and pink points have the same number of samples, the gray points are more widely distributed at the boundary, forming an unclear friction cone boundary, making the boundary fitting results unreliable. In contrast, the pink points are more concentrated, creating a clearer friction cone boundary, which enhances TacTID's performance in COSF estimation. Fig. 5(c) shows the COSF estimation results for TacTID and TacTip during frictional movement on the surfaces of nine materials. The maximum error for TacTID is 0.092, significantly smaller than TacTip's maximum absolute error of 0.39. In addition, across these nine materials, TacTID's mean

absolute error is 0.036, substantially lower than TacTip's mean absolute error of 0.194.

B. Effective Stiffness Estimation

To evaluate the effective stiffness estimation performance, TacTID is mounted on a vertical push-pull force gauge that carries TacTID to move vertically under closed-loop control to press ten silicone cubes of different effective Young's moduli [Fig. 5(a)]. For convenience, these ten silicone cubes are noted as S1, S2, ..., S10.¹

Throughout the experiment, the force gauge vertically propels TacTID to apply force feedback to the silicone cube from the starting point at a velocity of 10 mm/s . Once the pressure reaches the targeted values (20, 30, 40, 50, 60, 70, and 80 N), the force gauge stops and maintains a static position for 10 s, after which it returns to the initial position. Each silicone cube undergoes ten repetitions of identical presses. Fig. 6(b) depicts the interpolated pressure distribution of TacTID upon compressing silicone cubes S1, S4, S7, and S10 under a contact force of 30 N. The cyan area is the estimated contact area using (6) and the estimated contact area radii are indicated, while the optimized deformation distribution is shown under the interpolated result correspondingly. The results indicate that as the effective Young's modulus increases, the pressure distribution becomes increasingly concentrated and the radius of the contact area decreases. For silicone cubes with lower effective stiffness levels, the deformation distribution remains relatively uniform. According to (6), the contact area radius for each cube is determined by minimizing the estimation error of the pressure distribution using the gradient descent algorithm. Subsequently, knowing the optimized contact area radius, the effective Young's modulus of the corresponding silicone cube is calculated based on (7). As shown in Fig. 6(c), TacTID's predictions of the effective Young's modulus exhibit significant errors in the S8–S10 range. This occurs because when TacTID contacts harder objects, the contact force distribution becomes more concentrated, resulting in a smaller contact area predicted by the Hertzian theory and hence a smaller predicted contact area radius by (6), leading to higher relative errors for higher stiffness. In addition, TacTID also shows significant errors on S1 with relatively lower stiffness. The contact area predicted by the Hertzian theory exceeds the range of markers when TacTID is contacted with objects of lower stiffness, and

¹The corresponding effective Young's moduli are 0.621, 0.779, 1.391, 1.787, 2.135, 2.772, 3.322, 4.322, 5.067, and 5.379 MPa, respectively.

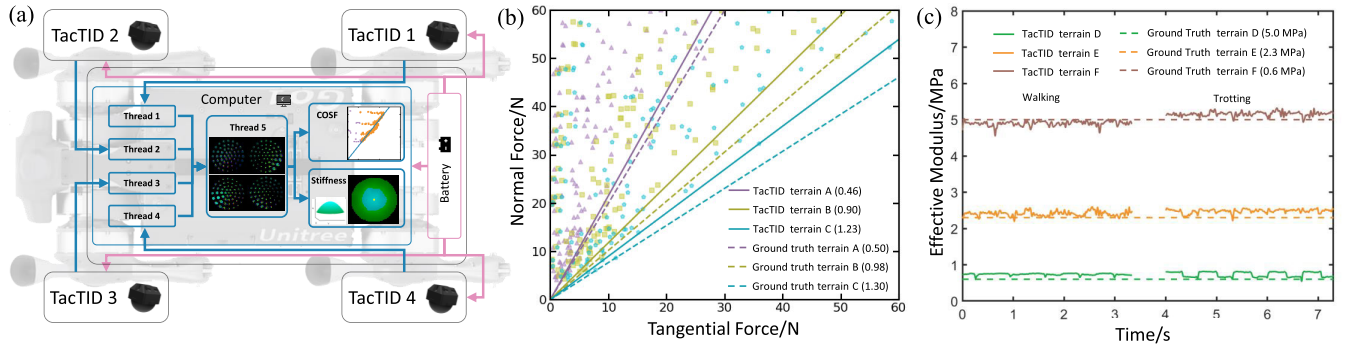


Fig. 7. Quadraped robot equipped with four TacTIDs. (a) Experimental setup and the workflow of the terrain identification on the quadruped robot with four TacTIDs. (b) Real-time COSF prediction results on three different terrains. (c) Real-time effective stiffness estimation results on three different terrains.

significant errors in the predicted contact area radius can occur. Overall, TacTID maintains a high stability with an average absolute error of 0.093.

C. Real-Time Quadraped Robot Implementation

To implement real-time terrain analysis on a quadruped, four TacTIDs are equipped to the feet of a Unitree Go1 robot and connected to an onboard Intel NUC (i7-1165G7 2.8-GHz CPU). As depicted in Fig. 7(a), the TacTIDs and NUC are powered by an onboard battery. This study aims to predict the COSF and effective stiffness of different terrains in real-time using the data captured from the TacTIDs. The raw output data from each TacTID are captured and processed in a separate thread to compute the normal force $F_{N,i}$, tangential force $F_{T,i}$, and the pressure distribution \mathbf{p}_i of each foot. With the aid of embedded markers and efficient feature extraction algorithms, each thread runs at a speed of 30 Hz. Thread 5 is used to collect the extracted features from all TacTIDs and calculate the terrain COSF and effective stiffness. During real-time COSF prediction, the friction is treated as the absolute value of the tangential force.

In the experimental results shown in Fig. 7(b), the terrains contacted by the four TacTIDs are considered the same, and all the samples are visualized together. Given that a larger portion of the data corresponds to scenarios with static friction forces rather than the sensor sliding on the robot arm, we decrease the value of m' to improve the fitting performance of the friction cone boundary. The final result of the COSF prediction is computed upon the sample set from all TacTIDs. Meanwhile, the quadruped robot is controlled, walking and trotting on three different terrains denoted as Terrains A, B, and C with COSF of 0.52, 0.98, and 1.30, respectively. Every time when there are new samples incoming, the predicted COSF is computed in real-time. Fig. 7(b) shows the prediction results of the three terrains. The average COSF prediction error of the three terrains is 0.06, and the lowest error is around 0.03 among these three terrains. A larger estimation error is observed in COSF estimation for rougher terrain, primarily due to the limited availability of data points around the friction cone. This limitation reduces the effectiveness of the estimation process.

For the effective stiffness prediction process, when the quadruped robot walks and trots on a terrain, Thread 5 acquires real-time pressure distribution and normal force, as depicted in Fig. 7(a). Data originating from a foot that is either

suspended or inadequately in contact with the terrain are deemed unreliable, necessitating the exclusion of such data at the commencement of each analysis. Given that the normal force tends toward 0 during suspension or insufficient contact, data where the normal force falls below a predefined threshold are disregarded. After the elimination of invalid data from multiple threads, the effective Young's modulus corresponding to each thread is computed individually. The effective stiffness is computed as the maximum of the effective Young's moduli of all valid data to avoid interference from dangling feet. In Fig. 7(c), a selected interval of the real-time predicted effective Young's modulus is visualized and compared with the ground truth. When the quadruped robot walks and trots on three different terrains denoted as Terrains D, E, and F with the effective Young's modulus of 0.6, 2.3, and 5.0 MPa, the average errors on the three terrains are less than 0.15 MPa. The prediction performs better in the walking state than the trotting state, which indicates the TacTID has higher accuracy with a lower velocity. The sharp transition of each real-time prediction typically occurs during the beginnings of the contact and detachment between the quadruped robot feet and the terrain. In this period, the contact between the feet and the terrain is unstable, resulting in larger prediction errors.

V. CONCLUSION

In this article, TacTID, a tactile sensor designed for high-resolution 3-D pressure distribution sensing on contact surfaces, is introduced. The elastic embedded marker array, with its significant area change, allows for direct inference of normal pressure. Experiments and simulations have shown that TacTID has higher normal pressure sensitivity compared with the conventional tactile sensor, TacTip. A standardized manufacturing process for TacTID has been proposed, ensuring its high repeatability. In addition, methods for terrain COSF estimation and effective stiffness prediction have been developed. The 3-D pressure distribution is used to accurately determine COSF in real-time through friction cone boundary fitting, while the effective stiffness estimation method uses the Hertzian theory to model the contact and fit the pressure distribution, estimating the contact effective Young's modulus with high accuracy. TacTID's potential applications for quadruped robots in terrain identification are also demonstrated. By equipping four TacTIDs on the feet of a quadruped robot, the friction and effective stiffness of different terrains can be predicted in

real-time. TacTID's sensing capabilities are primarily enabled by the elastic hemispherical shell and the embedded markers on its inner surface. By redesigning the adapter and adjusting the thickness of the elastic hemispherical shell, TacTID can be equipped and used on other legged robots. Given TacTID's high repeatability, it will also be deployed on other legged robots to demonstrate its compatibility and explore its potential on various legged robots, such as humanoid robots. In the future, the estimated COSF and stiffness information will be used to optimize the control policy of legged robots for more stable mobility on complex terrains. Overall, TacTID offers a promising solution for real-time tactile sensing and has potential applications in various fields, such as robotic sensing and human-machine interaction.

REFERENCES

- [1] T. Miki, J. Lee, J. Hwangbo, L. Wellhausen, V. Koltun, and M. Hutter, "Learning robust perceptive locomotion for quadrupedal robots in the wild," *Sci. Robot.*, vol. 7, no. 62, Jan. 2022, Art. no. eabk2822.
- [2] J. Man, G. Chen, and J. Chen, "Recent progress of biomimetic tactile sensing technology based on magnetic sensors," *Biosensors*, vol. 12, no. 11, p. 1054, Nov. 2022, doi: 10.3390/BIOS12111054.
- [3] C. Zhang, J. Zhang, J. Wu, and Q. Zhu, "Vision-assisted localization and terrain reconstruction with quadruped robots," in *Proc. IEEE/RSJ Int. Conf. Intell. Robots Syst. (IROS)*, Oct. 2022, pp. 13571–13577.
- [4] T.-Y. Lin, R. Zhang, J. Yu, and M. Ghaffari, "Legged robot state estimation using invariant Kalman filtering and learned contact events," in *Proc. Annu. Conf. Robot. Learn. (CoRL)*, Nov. 2021, pp. 1057–1066.
- [5] Y. Xu et al., "A flexible multimodal sole sensor for legged robot sensing complex ground information during locomotion," *Sensors*, vol. 21, no. 16, p. 5359, Aug. 2021.
- [6] H. Kolvenbach, C. Bärtschi, L. Wellhausen, R. Grandia, and M. Hutter, "Haptic inspection of planetary soils with legged robots," *IEEE Robot. Autom. Lett.*, vol. 4, no. 2, pp. 1626–1632, Apr. 2019.
- [7] A. G. Leal-Junior et al., "Polymer optical fiber for angle and torque measurements of a series elastic actuator's spring," *J. Lightw. Technol.*, vol. 36, no. 9, pp. 1698–1705, May 1, 2018.
- [8] A. Leal, V. Campos, A. Frizera, and C. Marques, "Low-cost and high-resolution pressure sensors using highly stretchable polymer optical fibers," *Mater. Lett.*, vol. 271, Jul. 2020, Art. no. 127810.
- [9] M. Y. Chuah and S. Kim, "Enabling force sensing during ground locomotion: A bio-inspired, multi-axis, composite force sensor using discrete pressure mapping," *IEEE Sensors J.*, vol. 14, no. 5, pp. 1693–1703, May 2014.
- [10] X. A. Wu, T. M. Huh, A. Sabin, S. A. Suresh, and M. R. Cutkosky, "Tactile sensing and terrain-based gait control for small legged robots," *IEEE Trans. Robot.*, vol. 36, no. 1, pp. 15–27, Feb. 2020.
- [11] N. D. W. Mudalige et al., "DogTouch: CNN-based recognition of surface textures by quadruped robot with high density tactile sensors," in *Proc. IEEE 95th Veh. Technol. Conf.*, Jun. 2022, pp. 1–5.
- [12] M. Y. M. Chuah, L. Epstein, D. Kim, J. Romero, and S. Kim, "Bi-modal hemispherical sensor: A unifying solution for three axis force and contact angle measurement," in *Proc. IEEE/RSJ Int. Conf. Intell. Robots Syst. (IROS)*, Macau, Nov. 2019, pp. 7968–7975.
- [13] N. Pestell and N. F. Lepora, "Artificial SA-I, RA-I and RA-II/vibrotactile afferents for tactile sensing of texture," *J. Roy. Soc. Interface*, vol. 19, no. 189, Apr. 2022, Art. no. 20210603.
- [14] H. B. Sun et al., "A soft thumb-sized vision-based sensor with accurate all-round force perception," *Nat. Mach. Intell.*, vol. 4, pp. 135–145, Feb. 2022.
- [15] W. Yuan, S. Dong, and E. H. Adelson, "GelSight: High-resolution robot tactile sensors for estimating geometry and force," *Sensors*, vol. 17, no. 12, p. 2762, 2017.
- [16] B. Ward-Cherrier et al., "The TacTip family: Soft optical tactile sensors with 3D-printed biomimetic morphologies," *Soft Robot.*, vol. 5, no. 2, pp. 216–227, 2018.
- [17] N. F. Lepora, "Soft biomimetic optical tactile sensing with the TacTip: A review," *IEEE Sensors J.*, vol. 21, no. 19, pp. 21131–21143, Oct. 2021.
- [18] L. Cramphorn, J. Lloyd, and N. F. Lepora, "Voronoi features for tactile sensing: Direct inference of pressure, shear, and contact locations," in *Proc. IEEE Int. Conf. Robot. Autom. (ICRA)*, May 2018, pp. 2752–2757.
- [19] T. Chan, "Point location in $o(\log n)$ time, Voronoi diagrams in $o(n \log n)$ time, and other transdichotomous results in computational geometry," in *Proc. 47th Annu. IEEE Symp. Found. Comput. Sci. (FOCS)*, Oct. 2006, pp. 333–344.
- [20] G. Zhang, Y. Du, Y. Zhang, and M. Y. Wang, "A tactile sensing foot for single robot leg stabilization," in *Proc. IEEE Int. Conf. Robot. Autom. (ICRA)*, May 2021, pp. 14076–14082.
- [21] E. A. Stone, N. F. Lepora, and D. A. W. Barton, "Walking on TacTip toes: A tactile sensing foot for walking robots," in *Proc. IEEE/RSJ Int. Conf. Intell. Robots Syst. (IROS)*, Oct. 2020, pp. 9869–9875.
- [22] N. Doshi, O. Taylor, and A. Rodriguez, "Manipulation of unknown objects via contact configuration regulation," in *Proc. Int. Conf. Robot. Autom. (ICRA)*, May 2022, pp. 2693–2699.
- [23] H. Hertz, "Über die berührung fester elastischer körper," *J. Fur Reine Angew. Math.*, vol. 92, no. 1881, pp. 156–171, 1881.
- [24] D. Rus and M. T. Tolley, "Design, fabrication and control of soft robots," *Nature*, vol. 521, no. 7553, pp. 467–475, May 2015.
- [25] S. Fahmi, M. Focchi, A. Radulescu, G. Fink, V. Barasuol, and C. Semini, "STANCE: Locomotion adaptation over soft terrain," *IEEE Trans. Robot.*, vol. 36, no. 2, pp. 443–457, Apr. 2020.
- [26] C. Chorley, C. Melhuish, T. Pipe, and J. Rossiter, "Development of a tactile sensor based on biologically inspired edge encoding," in *Proc. Int. Conf. Adv. Robot.*, Jun. 2009, pp. 1–6.
- [27] Q. Rabbani, A. Khan, and A. Qudus, "Modified Hungarian method for unbalanced assignment problem with multiple jobs," *Appl. Math. Comput.*, vol. 361, pp. 493–498, Nov. 2019.
- [28] S. Wang, Y. She, B. Romero, and E. Adelson, "Gelsight wedge: Measuring high-resolution 3D contact geometry with a compact robot finger," in *Proc. IEEE Int. Conf. Robot. Autom. (ICRA)*, May 2021, pp. 6468–6475.
- [29] M. A. Fischler and R. Bolles, "Random sample consensus: A paradigm for model fitting with applications to image analysis and automated cartography," *Commun. ACM*, vol. 24, no. 6, pp. 381–395, 1981.
- [30] S. Youssefian, N. Rahbar, and E. Torres-Jara, "Contact behavior of soft spherical tactile sensors," *IEEE Sensors J.*, vol. 14, no. 5, pp. 1435–1442, May 2014.
- [31] B. Audoly and Y. Pomeau, *Elasticity and Geometry: From Hair Curls to the Nonlinear Response of Shells*. London, U.K.: Oxford Univ. Press, 2010.
- [32] H. Hertz, "Über die berührung fester elastischer körper und über die harte," *Verh. Vereins Beford. Gewerbefleisscs*, no. 1882, pp. 449–463, 1882.
- [33] K. L. Johnson, *Contact Mechanics*. Cambridge, U.K.: Cambridge Univ. Press, 1987.



Ziwu Song received the B.S. (Hons.) degree in mechanical engineering from Nanjing University of Science and Technology, Nanjing, China, in 2020. He is currently pursuing the Ph.D. degree in data science and information technology with Tsinghua-Berkeley Shenzhen Institute, Tsinghua University, Beijing, China.

His research interests primarily revolve around robotic tactile sensing, robotic multimodal sensing, and application of tactile sensing in quadruped robots and embodied intelligence.



Chenchang Li (Graduate Student Member, IEEE) received the B.S. (Hons.) degree in automation from the University of Science and Technology of China, Hefei, China, in 2020, with the Special Class for the Gifted Young. He is currently pursuing the M.S. degree in data science and information technology with Tsinghua University, Beijing, China.

His research interests include robotics and machine learning.



Zhentan Quan is currently pursuing the M.E. degree in electronics and information with Tsinghua University, Beijing, China.

His research interests include robotics haptic perception and energy harvesting.



Shilong Mu received the B.S. degree in electronic information engineering from China University of Mining and Technology, Xuzhou, China, in 2022. He is currently pursuing the M.S. degree in data science and information technology with the Smart Sensing and Robotics (SSR) Group, Tsinghua University, Beijing, China.

His research interests include tactile sensing, electronic skin, and embodied AI.



Xiaosa Li (Graduate Student Member, IEEE) is pursuing the Ph.D. degree in data science and technology with Tsinghua-Berkeley Shenzhen Institute, Tsinghua University, Shenzhen, China.

His research interests include haptic interface and magnetic actuated robots.



Ziyi Zhao is pursuing the master's degree in data science and information technology with the School of Tsinghua-Berkeley Shenzhen Institute, Tsinghua University, Shenzhen, China.

His research interests include robotics sensing systems and algorithms.



Wanxin Jin received the Ph.D. degree from Purdue University, West Lafayette, IN, USA, in 2021.

He is an Assistant Professor with the School for Engineering of Matter, Transport, and Energy, Arizona State University, Tempe, AZ, USA. From 2021 to 2023, he held the position of Postdoctoral Researcher with the GRASP Lab, University of Pennsylvania, Philadelphia, PA, USA. He leads the Intelligent Robotics and Interactive Systems Lab, with Arizona State University.

His research interests include developing fundamental methods at the convergence of control, machine learning, and optimization, with the goal to enable robots to safely and efficiently interact with humans and physical objects.



Chenye Wu (Senior Member, IEEE) received the Ph.D. degree from the Institute for Interdisciplinary Information Sciences (IIIS), Tsinghua University, Beijing, China, in 2013.

His Ph.D. advisor is Prof. Andrew Yao, the Laureate of the A.M. Turing Award, in 2000. He is an Assistant Professor at the School of Science and Engineering, The Chinese University of Hong Kong (CUHK), Shenzhen, China. Before joining CUHK, he was an Assistant Professor at IIIS, Tsinghua University, Beijing, China. He worked

at ETH Zürich, Zürich, Switzerland, as a Wiss. Mitarbeiter (Research Scientist), working with Professor Gabriela Hug, in 2016. Before that, Prof. Kameshwar Poolla and Prof. Pravin Varaiya hosted him as

a Postdoctoral Researcher at the University of California at Berkeley, Berkeley, CA, USA, for two years. From 2013 to 2014, he spent one year at Carnegie Mellon University, Pittsburgh, PA, USA as a Postdoctoral Fellow, hosted by Prof. Gabriela Hug and Prof. Soumya Kar. He is currently working on data-driven power system operations.

Dr. Wu was the Best Paper Award co-recipient of IEEE SmartGridComm 2012, the IEEE PES General Meeting 2013, and the IEEE PES General Meeting 2020.



Wenbo Ding (Member, IEEE) received the B.S. and Ph.D. (Hons.) degrees from Tsinghua University, Beijing, China, in 2011 and 2016, respectively.

He worked as a Postdoctoral Research Fellow at Georgia Tech, Atlanta, GA, USA, under the supervision of Prof. Z. L. Wang, from 2016 to 2019. He is now an Associate Professor and Ph.D. Supervisor at Tsinghua-Berkeley Shenzhen Institute, Institute of Data and Information, Shenzhen International Graduate

School, Tsinghua University, where he leads the Smart Sensing and Robotics (SSR) Group. His research interests include diverse and interdisciplinary, which include self-powered sensors, energy harvesting, and wearable devices for health and robotics with the help of signal processing, machine learning, and mobile computing.

Dr. Ding has received many prestigious awards, including the Gold Medal of the 47th International Exhibition of Inventions Geneva and the IEEE Scott Helt Memorial Award.



Xiao-Ping Zhang (Fellow, IEEE) received the B.S. and Ph.D. degrees in electronic engineering from Tsinghua University, Beijing, China, in 1992 and 1996, respectively, and the M.B.A. (Hons.) degree in finance, economics and entrepreneurship from the University of Chicago Booth School of Business, Chicago, IL, USA, in 2008.

He is the Founding Dean of the Institute of Data and Information (iDI), Tsinghua Shenzhen International Graduate School (SIGS), Shenzhen, China, and the Chair Professor at Tsinghua SIGS and Tsinghua-Berkeley Shenzhen Institute (TBSI), Tsinghua University. He was with the Department of Electrical, Computer and Biomedical Engineering, Toronto Metropolitan University (Formerly Ryerson University), Toronto, ON, Canada, as a Professor, and the Director of the Communication and Signal Processing Applications Laboratory (CASPAL). He was the Program Director of Graduate Studies. He is a Registered Professional Engineer, ON, Canada. His research interests include statistical signal processing, image and multimedia content analysis, machine learning/AI/robotics, sensor networks and the IoT, and applications in big data, finance, and marketing.

Dr. Zhang is a Fellow of Canadian Academy of Engineering, and the Engineering Institute of Canada, and a member of Beta Gamma Sigma Honor Society. He was an Elected Member of the ICME Steering Committee. He is the General Co-Chair of the IEEE International Conference on Acoustics, Speech, and Signal Processing, in 2021, the 2017 GlobalSIP Symposium on Signal and Information Processing for Finance and Business, and the 2019 GlobalSIP Symposium on Signal, Information Processing and AI for Finance and Business. He is the General Chair of ICME2024. He served as a Senior Area Editor for IEEE TRANSACTIONS ON SIGNAL PROCESSING and an Associate Editor for IEEE TRANSACTIONS ON IMAGE PROCESSING, IEEE TRANSACTIONS ON MULTIMEDIA, IEEE TRANSACTIONS ON CIRCUITS AND SYSTEMS FOR VIDEO TECHNOLOGY, IEEE TRANSACTIONS ON SIGNAL PROCESSING, and IEEE SIGNAL PROCESSING LETTERS. He is a Senior Area Editor of IEEE TRANSACTIONS ON IMAGE PROCESSING. He is the Editor-in-Chief of IEEE JOURNAL OF SELECTED TOPICS IN SIGNAL PROCESSING. He was selected as IEEE Distinguished Lecturer by the IEEE Signal Processing Society and by the IEEE Circuits and Systems Society.